Letter

Improved Morphology and Efficiency of n-i-p Planar Perovskite Solar Cells by Processing with Glycol Ether Additives

Esma Ugur, Arif D. Sheikh, Rahim Munir, Jafar Iqbal Khan, Dounya Barrit, Aram Amassian, and Frédéric Laquai

ACS Energy Lett., **Just Accepted Manuscript** • DOI: 10.1021/acsenergylett.7b00526 • Publication Date (Web): 31 Jul 2017

Improved Morphology and Efficiency of n-i-p Planar Perovskite Solar Cells by Processing with Glycol Ether Additives

Esma Ugur, Arif D. Sheikh†, Rahim Munir, Jafar I. Khan, Dounya Barrit, Aram Amassian, Frédéric Laquai**

King Abdullah University of Science and Technology (KAUST), KAUST Solar Center (KSC), Physical Sciences and Engineering Division (PSE), Material Science and Engineering Program (MSE), Thuwal, 23955-6900, Kingdom of Saudi Arabia

Corresponding Authors

* Frédéric Laquai, Aram Amassian

Contact information: frederic.laquai@kaust.edu.sa, aram.amassian@kaust.edu.sa

†Present Address: School of Nanoscience and Technology, Shivaji University, Kolhapur 416 004, India

ABSTRACT

Planar perovskite solar cells can be prepared without high temperature processing steps typically associated with mesoporous device architectures; however, their efficiency has been lower and producing high quality perovskite films in planar devices has been challenging. Here, we report a modified two-step interdiffusion protocol suitable to prepare pin-hole free perovskite films with greatly improved morphology. This is achieved by simple addition of small amounts of glycol ethers to the preparation protocol. We unravel the impact the glycol ethers have on the perovskite film formation using in-situ UV-Vis absorbance and GIWAXS experiments. From these experiments we conclude: addition of glycol ethers changes the lead iodide to perovskite conversion dynamics and enhances the conversion efficiency, resulting in more compact polycrystalline films, and it creates micrometer-sized perovskite crystals vertically-aligned across the photoactive layer. Consequently, the average photovoltaic performance increases from 13.5% to 15.9% and reproduciability is enhanced, specifically when 2-methoxyethanol is used as additive.

TOC GRAPHICS

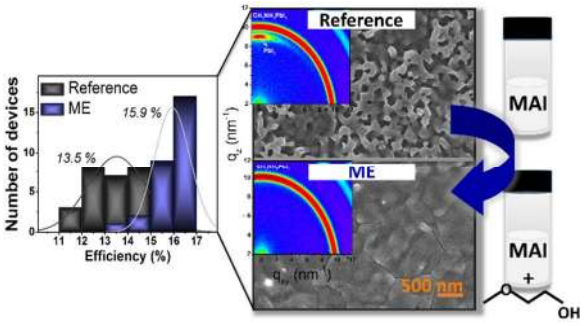

Metal halide perovskites have gained enormous attention as active materials in solution-processed photovoltaic devices. Since the first report of perovskite solar cells in 2009, the power conversion efficiency (PCE) has skyrocketed and meanwhile reached over 22% in less than a decade[1-3]. This rapid efficiency increase is remarkable and puts perovskite solar cells (PSCs) at the forefront of emerging photovoltaic (PV) technologies, which promise to be low-cost PV technologies that in the near future could help advance existing PV technologies[1] or even partially substitute them. The high efficiency of perovskite solar cells is attributed to the unique optical and electrical properties of perovskite absorbers such as large absorption coefficients across a wide spectral range, high carrier mobility, allowing micrometer long electron and hole diffusion lengths, and exciton binding energies on the order of k_BT[4-8]. Moreover, the perovskite layer has proven to be remarkably versatile and adoptable to different processing techniques, which include vacuum deposition and solution-processing[9-11]. Several different device architectures have been successfully used to fabricate highly-efficient solar cells, for instance, mesoporous scaffold structures as previously used for dye-sensitized solar cells and planar heterojunction structures with either n-i-p or p-i-n architectures, that is, n-type, intrinsic semiconductor, and p-type (n-i-p) or vice versa.[3, 12-15] To date, the highest device efficiency for PSCs has been reported for a mesoporous titania (TiO_2) scaffold used in the n-i-p device configuration, which requires high temperature (500 °C) sintering of the TiO_2 layer. Alternative, low temperature mesoporous organic electrodes have been successfully demonstrated in n-i-p devices[16], but planar device architectures which can be prepared at low temperatures are said to be more practical for large scale production of flexible and/or tandem solar cells [12, 17-20].

Enhancing the PCE of planar perovskite photovoltaic devices is the way forward not necessarily to compete with other established PV technologies such as silicon (Si), copper

indium gallium selenide (CIGS), and cadmium telluride (CdTe)[1, 21-22], but to make it compatible with these technologies, whose efficiencies could be boosted, when combined with a perovskite sub-cell in a tandem device structure[20, 23-25]. Amelioration of the perovskite film quality is one of the key parameters for highly efficient PSCs and several studies have addressed this issue. For example, solvent engineering was found to lead to high quality perovskite films when used in one-step and two-step deposition routes. Chen *et al.* simply added cyclohexane to the methylammonium iodide (MAI) solution to increase the photovoltaic performance of carbon electrode based PSCs. In this particular study, the authors claimed that the cyclohexane/MAI solvent mixture accelerated the conversion of lead iodide (PbI_2) to methylammonium lead iodide perovskite ($CH_3NH_3PbI_3$) resulting in a more complete perovskite coverage[26]. Furthermore, Jeon *et al.* reported that adding γ-butyrolactone (GBL) and dimethylsulphoxide (DMSO) to the precursor solutions in a one-step deposition gave highly uniform and compact perovskite layers[27]. Alternatively, PbI_2 was predissolved in N,N-dimethylformamide (DMF) and DMSO to form PbI_2·DMSO complexes[3, 28]. Another approach controlled the reaction of PbI_2 and MAI during an interdiffusion deposition using ethanol/isopropanol mixtures for MAI solutions[28]. This mixture was shown to have an impact on crystal growth as it changed the morphology of the perovskite thin films. A performance increase from ~11% to 15% was reported when using such ethanol-modified MAI solutions.

Besides solvent engineering, additives have been used to boost the device performance, for instance hypophosphorous acid (HPA), hydrochloric acid (HCl), or 1,8-diiodooctane (DIO)[29-31]. HPA addition led to remarkable improvements of the optoelectronic properties of $CH_3NH_3PbI_3$ perovskites[30]. Zhang *et al.* claimed that HPA-modified perovskites exhibited lower energetic disorder and reduced defect density due to enlarged perovskite grain sizes and a decreased

density of non-radiative recombination sites. Another example of controlling the morphology of perovskite films introduced polyethylene glycol (PEG) in perovskite precursor solutions[32-33]. It has been reported that the PEG scaffold stabilized the perovskite thin film due to the hygroscopicity of PEG molecules and their strong interaction with the perovskite itself[33]. Werner *et al.* have previously introduced 2-methoxyethanol as additive to reduce the surface roughness of perovskite absorber layers in monolithic tandem applications[20]. However, in their study PbI_2 was thermally evaporated. While more uniform and smooth perovskite thin films were obtained as compared to the control sample, the effect of 2-methoxyethanol on grain size or grain growth was not addressed.

In this study, we demonstrate that adding a small amount of a glycol ether, either 2-methoxyethanol (ME), 2-ethoxyethanol (EE), or 2-propoxyethanol (PE) (see **Table S1**), to the MAI solution prior to processing the perovskite thin film leads to compact, pin-hole free, and reproducible planar perovskite absorber layers when using a sequential two-step interdiffusion preparation protocol[11, 34]. This modification also led to improved conversion of PbI_2 to $CH_3NH_3PbI_3$ when comparing films prepared with and without glycol ether using otherwise similar processing conditions. Specifically, the addition of 2-methoxyethanol to the precursor solution resulted in improved perovskite crystal growth with an average grain size of up to 1 μm and vertically aligned crystals in a device structure. Furthermore, we observed a considerable enhancement of the average PCE (of 30 devices) from 13.5% to 15.9% with addition of 2-methoxyethanol. To gain further insight into the effect of glycol ether additives, we studied their impact on crystallization and film formation by time-resolved UV-Vis absorption spectroscopy and grazing incidence wide angle x-ray scattering (GIWAXS) measurements.

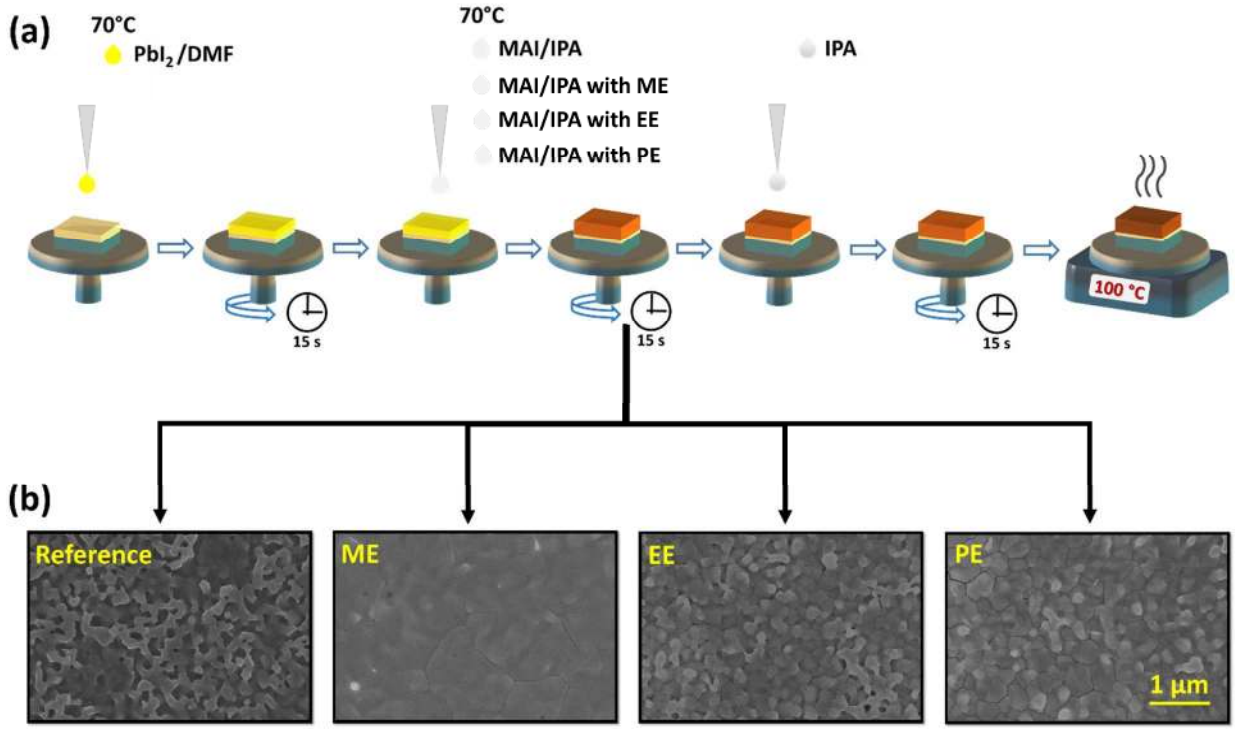

Figure 1. (a) Schematic representation of the perovskite layer deposition process used in this work, starting with spin-coating of PbI_2 from DMF solution, followed by MAI loading, IPA washing, and thermal annealing. The glycol ethers are: 2-methoxyethanol (ME), 2-ethoxyethanol (EE), and 2-propoxyethanol (PE). **(b)** SEM micrographs of the final $CH_3NH_3PbI_3$ perovskite absorber layers prepared with different glycol ether additives in MAI solution (scale bar: 1 µm). Micrographs were obtained after washing and thermal annealing steps were completed.

The one-step preparation of $CH_3NH_3PbI_3$ layers has previously been investigated by in-situ diagnostics and was shown to proceed through the formation of disordered and crystalline precursor solvates, which template the final film morphology[35-36]. The two-step perovskite layer preparation is expected to allow better control during the fabrication of the perovskite active layer[37]. However, the formation of the PbI_2 film itself is rather complex, involving formation of disordered and crystalline PbI_2·DMF solvate complexes, which convert in ambient conditions

and ultimately seed the PbI_2 phase after only ~5 mins in ambient air[38]. Therefore, the precise timing of the two-step protocol matters to the overall conversion process. Here, we have used the sequential interdiffusion protocol shown in **Figure 1a** to fabricate perovskite thin films. We note that the as-cast PbI_2 film was spin-cast from DMF solution for a duration of 15 s and immediately after exposed to the MAI solution in IPA without prior thermal annealing. This insures the as-cast PbI_2 film consists in fact of PbI_2·DMF complexes at the time of MAI loading, as evidenced from *in-situ* GIWAXS and optical absorbance measurements (**Figure S1**)[38]. To tune the perovskite layer's conversion process, a small amount of a glycol ether, either ME, EE or PE, was added to the MAI solutions used in the preparation of the second stack layer. Scanning electron microscopy (SEM) images of the perovskite samples are shown in **Figure 1b**. Clearly, the addition of a glycol ether to the MAI precursor solution in IPA affected the morphology of the perovskite layers obtained after washing and thermal annealing. In fact, more compact and uniform perovskite thin films were obtained for either additive compared to the reference sample (**Figure S2**). Particularly, the use of ME as additive resulted in enlarged average grain sizes of up to 1 μm and in addition led to uniform crystal growth all across the vertical axis of the thin perovskite film. Furthermore, the impact of the quantity of the additive on the perovskite film morphology was also studied by adding different amounts of glycol ethers from 1-5% (v/v) to the MAI/IPA precursor solution. SEM micrographs of the samples prepared with different quantities of glycol ethers can be found in the Supporting Information (**Figure S3**). Clearly, all glycol ether additives facilitated the perovskite grain growth. However, while adding more glycol ether resulted in larger perovskite grains, the surface morphology of the perovskite film deteriorated when more than 3% (v/v) were added. The surface roughness of the perovskite thin films was investigated by atomic force microscopy (AFM) shown in **Figure S4.**

As expected, addition of 2-methoxyethanol reduced the surface roughness of the perovskite thin films to about 20 nm, while the reference sample (the one without additive) had an average surface roughness of 30 nm.

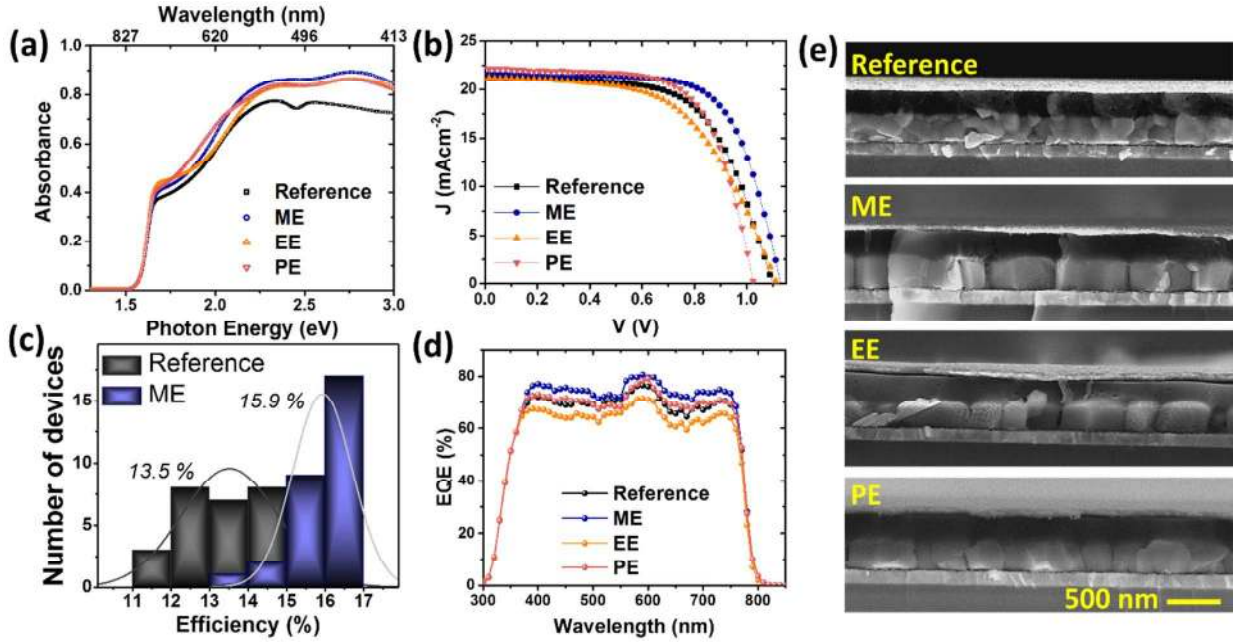

Figure 2. (a) UV-Vis absorption spectra of $CH_3NH_3PbI_3$ perovskite absorber layers prepared with different glycol ether additives, **(b)** J-V characteristics of planar $CH_3NH_3PbI_3$ perovskite solar cells measured in reverse sweep mode, **(c)** histogram of PCEs for reference devices and ME devices based on reverse J-V sweeps, **(d)** EQE measurements of reference device and devices prepared with glycol ethers, and **(e)** cross-sectional SEM images of all $CH_3NH_3PbI_3$ perovskite photovoltaic devices (scale bar: 500 nm).

After annealing of the perovskite thin films, steady-state UV-Vis measurements were performed (**Figure 2a**). These experiments showed a remarkable increase of the absorbance in the visible region for perovskite films prepared with glycol ethers. We attribute this effect to the high quality of perovskite crystals in the layer, and confirmed that the thickness of the perovskite layers was not altered due to the addition of the glycol ether, being in all cases 300±30 nm, as

measured by cross sectional SEM. The band gap of all perovskite layers was determined to be 1.60±0.02 eV using a Tauc plot, confirming that the glycol ether addition did not alter the band gap either (**Figure S5**).

Table 1. Figures of merit of $CH_3NH_3PbI_3$ perovskite solar cells (ITO/ZnO/$MAPbI_3$/spiro-OMeTAD/MoO_x/Ag) prepared with different glycol ether additives. Shown here are average values of 30 devices and the highest device efficiency obtained.

Sample	J_{sc} (mA cm^{-2})	V_{oc} (V)	FF (%)	η (%)	$\eta_{champion}$ (%)
Ref	21.5±0.7	1.09±0.02	58±3.8	13.5±1.3	14.3
ME	21.9±0.4	1.12±0.02	65±3.0	15.9±0.8	16.7
EE	21.1±0.4	1.07±0.03	54±4.8	11.8±1.2	13.2
PE	21.2±0.5	1.08±0.02	62±2.9	13.9±1.2	15.1

Planar perovskite solar cells of the structure ITO/ZnO/$MAPbI_3$/spiro-OMeTAD/MoO_x/Ag (n-i-p structure) were prepared to investigate the impact of glycol ethers and improved perovskite thin film morphology on device performance (**Figure 2b** and **Table S2-S4**). Interestingly, the short circuit current densities (J_{sc}) were similar across the series of devices, in between 21 – 22 mA cm^{-2}, despite the increased absorbance. However, a slight improvement in open circuit voltage (V_{oc}) from 1.11 to 1.13 V was observed, when ME was used. More importantly, the fill factor (FF) increased from 62% to 68% resulting in an overall enhancement of the average PCE from 13.5% for the reference sample to 15.9% for the device prepared with ME (**Table 1**). Furthermore, the highest efficiency obtained for the sample prepared with ME was 16.7%, while

it was 14.3% for the reference samples prepared without glycol ether. The distribution of efficiencies for 30 reference samples and 30 devices prepared with ME is depicted in **Figure 2c.** Moreover, detailed device statistics for J_{sc}, V_{oc} and FF of all samples can be found in **Figure S6**. Besides the increase in device performance a narrower efficiency distribution for ME samples is observed. The external quantum efficiency (EQE) spectra for representative reference and devices prepared with additives are presented in **Figure 2d**. Furthermore, we note that the addition of glycol ether has a positive impact on the hysteresis typically associated with planar n-i-p device structures, when using ZnO electron transport layers. In fact, the hysteresis was significantly reduced in the sample prepared with ME compared to the reference sample as can be seen from **Figure S7**; yet, we did not manage to completely suppress the hysteresis, which has to be addressed in future work.

We hypothesize the efficiency improvement is primarily linked to morphological improvements, specifically the enlarged perovskite grain size, especially in the vertical direction across the photoactive layer, when using ME, as confirmed by cross-sectional SEM images (**Figure 2e**). The formation of larger grains in the vertical direction reduces the number of grain boundaries which could potentially hinder charge transport and act as traps, as photogenerated electrons and holes must diffuse across the layer to reach the charge collection electrodes. This effect is well-known to limit device performance.[39-40] Similarly, the use of PE also enhanced device performance, however, only moderately up to a highest PCE of 15.1%. In stark contrast, no improvement in device performance was observed when EE was used. In fact, we observed by eye that the color of the perovskite layer with EE changed from brown to fawn after annealing of the perovskite on ZnO/ITO. The results strongly indicate that this is a consequence of the instability of the ZnO/perovskite interface as also witnessed earlier[41-42].

The morphological and device data clearly demonstrated that adding glycol ethers in the conversion from PbI_2 to perovskite affects significantly the grain growth and quality of the perovskite absorber layer. To shed more light on the mechanism of the two-step perovskite formation process and to better understand the influence of the additive during the conversion of the PbI_2 precursor film, we performed multiprobe *in-situ* diagnostics during PbI_2 spin-coating, as well as during its subsequent solution-phase and thermal conversion (see also scheme in **Figure 1**). In **Figure S1a** we show a two-dimensional (2D) GIWAXS measurement taken during spin-coating of the PbI_2 from DMF solution at 15 s. The GIWAXS data indicate that the initially wet precursor film is primarily dry at the 15 s mark using a fast coating speed of 3500 rpm, as indicated by the loss of the liquid phase solvent scattering halo at high q, and by the transformation of the small and intermediate angle scattering halo (< 8 nm^{-1}) into diffraction peaks associated to an ordered PbI_2·DMF sol-gel precursor. Absence of the crystalline PbI_2 phase scattering feature (9.1 nm^{-1}) is noteworth and in agreement with our previous observations, according to which PbI_2 formation at room temperature can occur after several minutes of drying in air[38]. Furthermore, we performed in-situ UV-Vis absorption measurements during PbI_2 spin-coating using a home-built combination of a spin coater and *in-situ* UV-Vis spectrophotometer described earlier[43]. The time-resolved ground state absorption spectra were calculated from the respective transmission spectra using the following equation: $A_\lambda = -log_{10}(T)$ where A_λ is the absorbance at a certain wavelength λ and T is the intensity of the calibrated transmitted light[43]. The band edge of the solvated crystalline PbI_2·DMF film at 30 s (**Figure S1b**) is significantly red-shifted (~450 to ~460 nm) with respect to the disordered and wet sol-gel state measured at 1 s (~420 nm). The PbI_2 film formed after thermal annealing showed the expected characteristics of the yellowish material, exhibiting a further significant redshift to ~530 nm. It is therefore clear

that the conversion of PbI_2 into the perovskite phase occurs primarily from a PbI_2·DMF complex crystalline phase exhibiting an expanded lattice thanks to solvation, and shown to be unstable, with a lifetime of only minutes at room temperature[38].

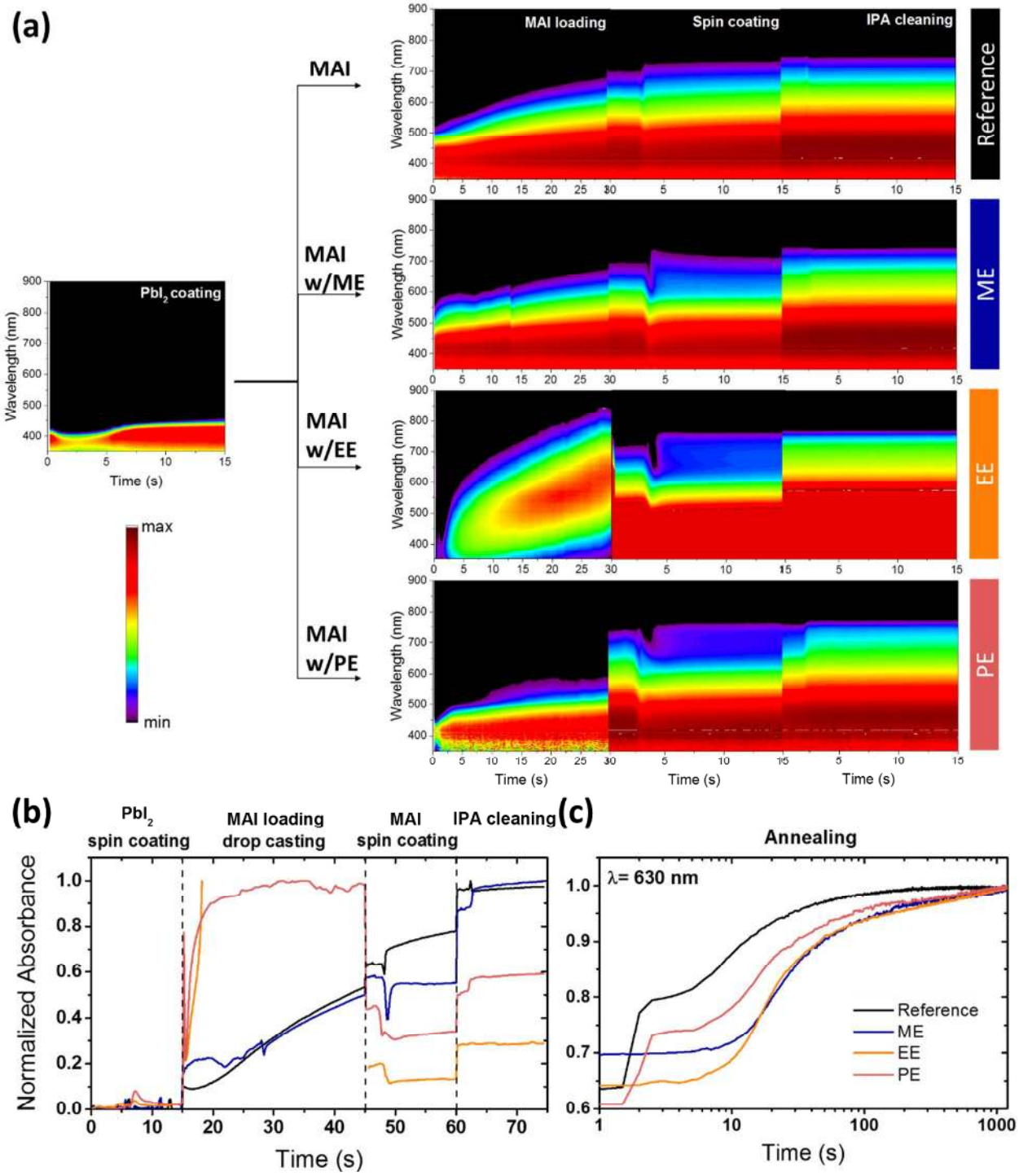

Figure 3. (a) 2D color maps showing the spectral evolution of the UV-Vis absorption of the reference and glycol ether samples during spin-coating. The subsections of the plot show from the left to the right: sequential deposition of the PbI_2 layer, MAI loading, spin coating of the MAI layer, and IPA cleaning, respectively. **(b-c)** Temporal evolution of the UV-Vis absorption at λ= 630 nm during the different stages of PbI_2 deposition, MAI loading using different additives, and various spin coating stages and during thermal annealing following solution-phase conversion of the as-cast PbI_2 film using different additives.

We also investigated further the solution-phase and thermal conversion steps by performing *in situ* UV-Vis absorption measurements during MAI loading of the PbI_2·DMF complex precursor film, as well as during the subsequent spin-off of the excess MAI, IPA wash, and subsequent thermal annealing. In **Figure 3a** we show a 2D color maps of the temporal evolution of the UV-Vis absorption spectra for all four conversion conditions (i.e. reference and three different glycol ether additives) during each of the aforementioned steps. In the first step, the formation of a solid-state PbI_2·DMF precursor film is observed within 15 s during spin coating at 3500 rpm, as indicated by the significantly blue-shifted absorption edge compared to solid state PbI_2 (see **Figure S1b**). The conversion of the as-cast precursor film started immediately upon drop-casting of the MAI solution, as indicated by the increasing absorbance and gradual red-shift of the absorption edge from that of solvated PbI_2 towards that of solid state $CH_3NH_3PbI_3$. To monitor the perovskite layer formation and reaction progress, we plotted in **Figure 3b** the absorbance at λ = 630 nm as a function of the process time, as at that wavelength primarily the perovskite absorbs. This analysis ignores any non-idealities from light scattering and light coupling distortion which may be present due to the curved liquid droplet, especially during loading periods. The absorbance at this wavelength increases steadily in time for both the

reference and ME sample during MAI loading. In contrast, in the presence of EE we saw a pronounced rapid rise of the absorbance due to an apparently fast conversion during the loading stage. We suspect the excessively rapid process prevents completion of the conversion of the precursor film and may be the primary reason for its instability and color change observed upon annealing. Subsequent spin-off of the excess solution causes stabilization in the case of ME, while EE and PE exhibit a further slow rise of the absorbance. During IPA cleaning, no further change of the absorbance was observed for the reference and EE samples, while a significant increase in absorbance occurred for the ME and PE sample. The in-situ absorption measurements reveal also that the samples exhibited different PbI_2 to $CH_3NH_3PbI_3$ conversion dynamics. In particular, the ME sample showed largely altered conversion characteristics compared to the reference sample, converting significantly during the IPA washing step as opposed to the reference, ultimately achieving similar absorbance as the reference sample at λ= 630 nm.

In-situ UV-Vis absorption measurements performed during the annealing step of the perovskite thin films are shown in **Figure 3c** on a semilogarithmic scale. We observed significant differences in the change of normalized absorbance for the reference and modified samples after glycol ether addition. The reference sample exhibited a rapid increase of absorbance with annealing, increasing to 95% of its final absorbance within 60 s. In contrast, the glycol ether addition slowed down the perovskite formation during annealing, with the exception of PE. The absorbance in the presence of ME increased to 72% within the first minute. Changes in absorbance were found to be comparably slow in case of EE during annealing, while a faster change was observed between 10 to 40 s for the case of EE (**Figure 3c**). These results indicate that conversion to the tetragonal perovskite phase is more controlled during the annealing step, when ME is used as additive during the MAI loading. In order to further understand the grain

growth mechanism, we took SEM images of the reference and ME samples at increasing annealing times (t=0, 10, 90 and 300 s) (**Figure S8**). The SEM micrographs of the reference and ME samples prior to annealing are clearly different in terms of nucleation of grains and thin film structure, which implies different solid-solid reaction dynamics between MAI and PbI_2 during spin coating[44-45]. While the reference sample exhibited smaller grains and pin holes at t=0 s, the ME film was more compact and virtually pin-hole free. The temporal evolution of the UV-Vis absorption combined with the information from SEM micrographs (**Figure 3** and **S8**) indicates rapid conversion and crystallization in the absence of glycol ether additives. A better controlled conversion in ME samples resulted in smaller grains with concave and convex grain boundaries. We observed at different annealing times that grains with concave grain boundaries grew towards adjacent grains with convex grain boundaries. In fact, the SEM images indicate that a controlled solid-state grain growth mechanism is the dominant process in the ME samples in turn leading to thin films with large grains compared to the vertical film thickness[45].

Static GIWAXS measurements performed on the annealed samples immediately after the conversion are presented in **Figure 4a**. The data reveals a powder ring associated to the (110) reflection of the perovskite phase, indicating that in all cases it is predominantly formed with random orientation, with a more prominent preference for out-of-plane orientation when additives are used, as indicated by the azimuthal intensity distribution of the perovskite powder ring in **Figure 4c**. The reference sample appears to have undergone incomplete conversion as indicated by the presence of a rather sharp PbI_2 peak. The latter is highly textured in the out-of-plane direction indicating that the PbI_2 phase is probably templated either at the top surface or the bottom interface. Static GIWAXS measurements were also performed at different angles of incidence, both above and below the critical angle of the perovskite. The relative intensity of the

PbI_2 peak decreases with respect to the perovskite ring in shallower angle conditions, suggesting the PbI_2 phase is predominantly found at the buried interface. All other samples prepared with glycol ether additives showed complete conversion to perovskite.

In **Figure S9** we compare the *ex-situ* X-ray diffraction (XRD) spectra in the Bragg-Bentano configuration (longitudinal) for the reference perovskite thin films with those prepared with different glycol ether additives and with a neat PbI_2 film. The longitudinal section of the perovskite main peak is observed at around $2\theta=14.7°$ for (110) and its intensity increased upon use of glycol ethers, in agreement with the GIWAXS pole-figures. All perovskite thin films have additional diffraction peaks around 28.7° and 32.4° assigned to the (220) and (310) perovskite crystal planes, respectively[46]. Another important feature seen in the XRD spectra is the PbI_2 peak at around $2\theta=13.2°$, which was present in all samples, unlike in GIWAXS measurements performed *ex-situ* on samples that were rigorously kept under nitrogen, as XRD measurements were typically performed several hours after sample preparation and tend to be more sensitive to the bulk of the film. The peak intensity was clearly reduced when glycol ethers were used during film formation. The ME sample exhibited the lowest PbI_2 peak intensity, indicating perovskite conversion from PbI_2 is more complete upon addition of ME. We note that several studies have indicated that the presence of PbI_2 has an impact on device performance[47-48]. Therefore, better control over the PbI_2 content as shown through the use of glycol ether additives is also likely to help achieve improved solar cell performance. We also investigated whether any residual glycol ether molecules remained in the perovskite absorber layers by performing Fourier transform infrared (FT-IR) spectroscopy (**Figure S10**), and found that after annealing of the perovskite layer the main peaks from glycol ether molecules had disappeared.

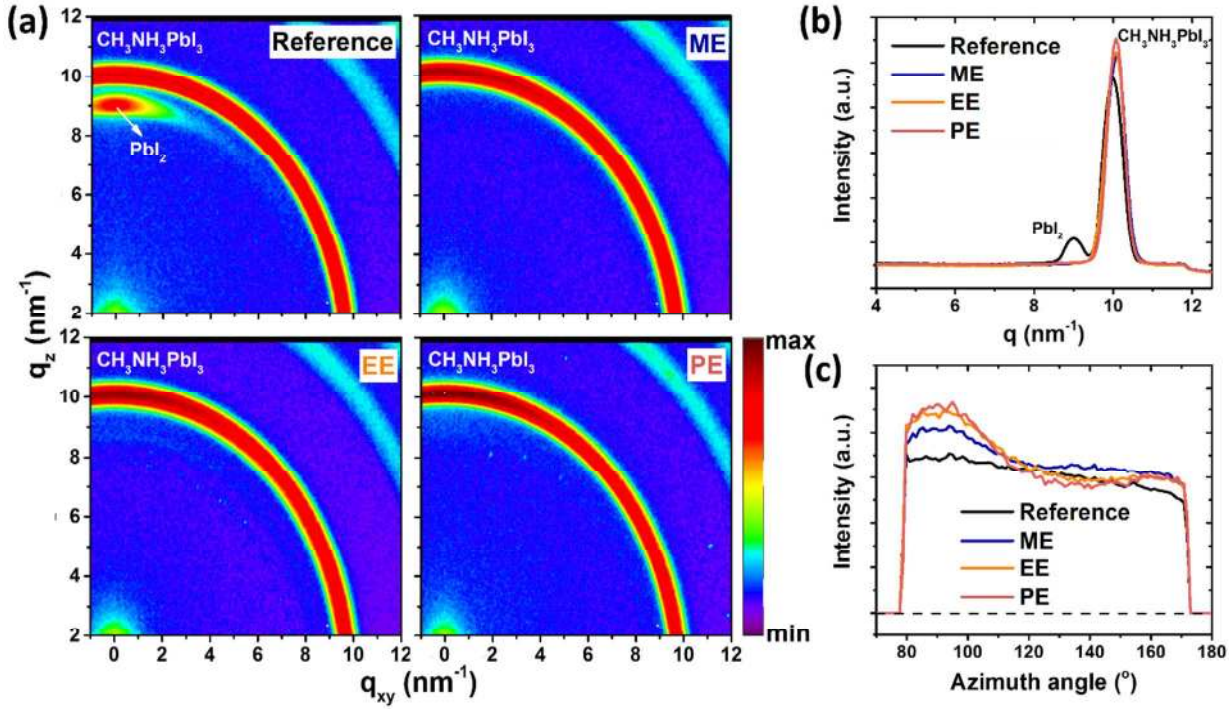

Figure 4. (a) 2D-GIWAXS spectra of $CH_3NH_3PbI_3$ perovskite absorber layers prepared with different glycol ether additives, **(b)** azimuthally integrated 1D-plots showing the signal intensity versus q (nm^{-1}), and **(c)** the azimuthal-angle intensity of the q=10 nm^{-1} peak from GIWAXS for $CH_3NH_3PbI_3$ perovskite absorber layers after annealing.

In summary, the addition of glycol ether molecules to the MAI solution in a two-step perovskite thin film preparation alters the lead iodide to perovskite conversion dynamics and thin film morphology, ultimately resulting in enlarged grain sizes of up to 1 µm across the entire perovskite film. We observed that glycol ethers affect the dynamics of grain growth during the sequential interdiffusion deposition protocol, slowing it down and promoting slower, but more complete conversion. In-depth studies performed by in-situ absorption spectroscopy were used to confirm the impact of additives on the conversion dynamics of PbI_2 to perovskite. Furthermore, we observed that glycol ether addition increases the absorbance of as-converted perovskite thin films as demonstrated by UV-Vis absorption spectroscopy measurements. Enhanced absorbance

of perovskite thin films at similar film thicknesses is attributed to improved lead iodide to perovskite conversion and perovskite crystal quality. Moreover, both XRD and GIWAXS results demonstrated an increased conversion yield of PbI_2 to $CH_3NH_3PbI_3$ when using glycol ether molecules as additives. Furthermore, vertically-aligned perovskite crystals with fewer grain boundaries were observed in cross-sectional SEM imaging. The addition of glycol ethers thus induced not only improved perovskite film morphology, but also a remarkable change in device performance with maximum efficiencies up to 16.7% and an overall narrower efficiency distribution, in other words, better reproducibility of the device performances. The narrower distribution at higher efficiency is attributed to better control of the thin film growth, when using glycol ether molecules as additives. In short, adding a small amount of ME during the preparation of the perovskite absorber layer appears to be a promising route to achieve higher quality perovskite polycrystalline films and it paves the way towards more efficient planar perovskite photovoltaic devices when applying a two-step deposition protocol.

Finally, we emphasize that better morphology control is very important for studies that address in more depth the correlation between perovskite composition, processing conditions, film morphology, and photopysical properties, which ultimately determine the device performance[49]. For instance, advanced spectroscopic and imaging techniques such as Kelvin probe force microscopy (KPFM), photocurrent AFM (pcAFM), piezoresponse force microscopy (PFM), and electron beam-induced current (EBIC) experiments are extremely valuable tools that can probe the electrical response of individual grains of the $MAPbI_3$ perovskite films prepared with glycol ether additives[49-51]. Spatially-resolved transient micro-photoluminescence (μ-PL) imaging is one of the key techniques to probe the carrier dynamics locally within grains, close to the grain

boundaries, and across the grain boundaries[30, 52]. Lastly, light-induced degredation and the effect of atmospheric conditions can be investigated using *in-situ* structural analysis techniques[53].

ASSOCIATED CONTENT

Supporting Information.

Experimental details and supplementary characterizations of materials and device performance.

AUTHOR INFORMATION

Corresponding Authors

*E-mail: frederic.laquai@kaust.edu.sa; aram.amassian@kaust.edu.sa

Webpage:

Ultrafast Dynamics Group: https://ufd.kaust.edu.sa

Orcid:

Esma Ugur: 0000-0003-0070-334X

Arif D. Sheikh: 0000-0003-3823-0947

Rahim Munir: 0000-0002-6029-3760

Jafar I. Khan: 0000-0001-6003-5641

Aram Amassian: 0000-0002-5734-1194

Frédéric Laquai: 0000-0002-5887-6158

Notes

The authors declare no competing financial interest.

ACKNOWLEDGMENTS

This work was supported by the King Abdullah University of Science and Technology (KAUST). GIWAXS measurements were performed at D-line at the Cornell High Energy Synchrotron Source (CHESS) at Cornell University. CHESS is supported by the NSF & NIH/NIGMS via NSF award DMR-1332208.

REFERENCES

(1) Green, M. A.; Emery, K.; Hishikawa, Y.; Warta, W.; Dunlop, E. D. Solar Cell Efficiency Tables (version 48). *Prog. Photovoltaics: Research and Applications* **2016,** *24*, 905-913.
(2) Kojima, A.; Teshima, K.; Shirai, Y.; Miyasaka, T. Organometal Halide Perovskites as Visible-Light Sensitizers for Photovoltaic Cells. *J. Am. Chem. Soc.* **2009,** *131*, 6050-6051.
(3) Yang, W. S.; Noh, J. H.; Jeon, N. J.; Kim, Y. C.; Ryu, S.; Seo, J.; Seok, S. I. High-Performance Photovoltaic Perovskite Layers Fabricated Through Intramolecular Exchange. *Science* **2015,** *348*, 1234-1237.
(4) Stranks, S. D.; Eperon, G. E.; Grancini, G.; Menelaou, C.; Alcocer, M. J. P.; Leijtens, T.; Herz, L. M.; Petrozza, A.; Snaith, H. J. Electron-Hole Diffusion Lengths Exceeding 1 Micrometer in an Organometal Trihalide Perovskite Absorber. *Science* **2013,** 342, 341-344.
(5) De Wolf, S.; Holovsky, J.; Moon, S. J.; Loper, P.; Niesen, B.; Ledinsky, M.; Haug, F. J.; Yum, J. H.; Ballif, C. Organometallic Halide Perovskites: Sharp Optical Absorption Edge and Its Relation to Photovoltaic Performance. *J. Phys. Chem. Lett.* **2014,** *5*, 1035-1039.
(6) Wang, Y.; Zhang, Y.; Zhang, P.; Zhang, W. High Intrinsic Carrier Mobility and Photon Absorption in The Perovskite $CH_3NH_3PbI_3$. *Phys. Chem. Chem. Phys.* **2015,** *17*, 11516-11520.
(7) Lin, Q.; Armin, A.; Nagiri, R. C. R.; Burn, P. L.; Meredith, P. Electro-Optics of Perovskite Solar Cells. *Nat. Photonics* **2014,** *9*, 106-112.
(8) Saba, M.; Quochi, F.; Mura, A.; Bongiovanni, G. Excited State Properties of Hybrid Perovskites. *Acc. Chem. Res.* **2016,** *49*, 166-173.
(9) Liu, M.; Johnston, M. B.; Snaith, H. J. Efficient Planar Heterojunction Perovskite Solar Cells by Vapour Deposition. *Nature* **2013,** *501*, 395-398.
(10) Chen, Q.; Zhou, H.; Hong, Z.; Luo, S.; Duan, H.-S.; Wang, H.-H.; Liu, Y.; Li, G.; Yang, Y. Planar Heterojunction Perovskite Solar Cells via Vapor-Assisted Solution Process. *J. Am. Chem. Soc.* **2014,** *136*, 622–625.
(11) Xiao, Z.; Bi, C.; Shao, Y.; Dong, Q.; Wang, Q.; Yuan, Y.; Wang, C.; Gao, Y.; Huang, J. Efficient, High Yield Perovskite Photovoltaic Devices Grown by Interdiffusion of Solution-Processed Precursor Stacking Layers. *Energy Environ. Sci.* **2014,** *7*, 2619-2623.
(12) Eperon, G. E.; Stranks, S. D.; Menelaou, C.; Johnston, M. B.; Herz, L. M.; Snaith, H. J. Formamidinium Lead Trihalide: A Broadly Tunable Perovskite for Efficient Planar Heterojunction Solar Cells. *Energy Environ. Sci.* **2014,** *7*, 982-988.

(13) Meng, L.; You, J.; Guo, T. F.; Yang, Y. Recent Advances in The Inverted Planar Structure of Perovskite Solar Cells. *Acc. Chem. Res.* **2016,** *49*, 155-165.
(14) Saliba, M.; Matsui, T.; Seo, J. Y.; Domanski, K.; Correa-Baena, J. P.; Nazeeruddin, M. K.; Zakeeruddin, S. M.; Tress, W.; Abate, A.; Hagfeldt, A.; *et al.* Cesium-Containing Triple Cation Perovskite Solar Cells: Improved Stability, Reproducibility and High Efficiency. *Energy Environ. Sci.* **2016,** *9*, 1989-1997.
(15) Zhou, Z.; Pang, S.; Liu, Z.; Xu, H.; Cui, G. Interface Engineering for High-Performance Perovskite Hybrid Solar Cells. *J. Mater. Chem. A* **2015,** *3*, 19205-19217.
(16) Zhong, Y.; Munir, R.; Balawi, A. H.; Sheikh, A. D.; Yu, L.; Tang, M.-C.; Hu, H.; Laquai, F.; Amassian, A. Mesostructured Fullerene Electrodes for Highly Efficient n–i–p Perovskite Solar Cells. *ACS Energy Lett.* **2016,** *1*, 1049–1056.
(17) Yoon, H.; Kang, S. M.; Lee, J.-K.; Choi, M. Hysteresis-Free Low-Temperature-Processed Planar Perovskite Solar Cells with 19.1% Efficiency. *Energy Environ. Sci.* **2016,** *9*, 2262-2266.
(18) Liu, D.; Kelly, T. L. Perovskite Solar Cells with a Planar Heterojunction Structure Prepared Using Room-Temperature Solution Processing Techniques. *Nat. Photonics* **2014,** *8*, 133–138.
(19) Wu, Y.; Yang, X.; Chen, W.; Yue, Y.; Cai, M.; Xie, F.; Bi, E.; Islam, A.; Han, L. Perovskite Solar Cells with 18.21% Efficiency and Area Over 1 Cm^2 Fabricated by Heterojunction Engineering. *Nat. Energy* **2016,** *1*, 1-7.
(20) Werner, J.; Weng, C.-H.; Walter, A.; Fesquet, L.; Seif, J. P.; De Wolf, S.; Niesen, B.; Ballif, C. Efficient Monolithic Perovskite/Silicon Tandem Solar Cell with Cell Area >1 cm^2. *J. Phys. Chem. Lett.* **2016,** *7*, 161–166.
(21) Polman, A.; Knight, M.; Garnett, E. C.; Ehrler, B.; Sinke, W. C. Photovoltaic Materials: Present Efficiencies and Future Challenges. *Science* **2016,** *352*, aad4424.
(22) Jackson, P.; Wuerz, R.; Hariskos, D.; Lotter, E.; Witte, W.; Powalla, M. Effects of Heavy Alkali Elements in Cu(In,Ga)Se_2 Solar Cells with Efficiencies up to 22.6%. *Phys. Status Solidi RRL* **2016,** *10*, 583-586.
(23) Bailie, C. D.; Christoforo, M. G.; Mailoa, J. P.; Bowring, A. R.; Unger, E. L.; Nguyen, W. H.; Burschka, J.; Pellet, N.; Lee, J. Z.; Grätzel, M.; *et al.* Semi-Transparent Perovskite Solar Cells for Tandems with Silicon and CIGS. *Energy Environ. Sci.* **2015,** *8*, 956-963.
(24) Fu, F.; Feurer, T.; Weiss, T. P.; Pisoni, S.; Avancini, E.; Andres, C.; Buecheler, S.; Tiwari, A. N. High-Efficiency Inverted Semi-Transparent Planar Perovskite Solar Cells in Substrate Configuration. *Nat. Energy* **2016,** *2,* 16190.
(25) Werner, J.; Barraud, L.; Walter, A.; Bräuninger, M.; Sahli, F.; Sacchetto, D.; Tétreault, N.; Paviet-Salomon, B.; Moon, S.-J.; Allebé, C.; *et al.* Efficient Near-Infrared-Transparent Perovskite Solar Cells Enabling Direct Comparison of 4-Terminal and Monolithic Perovskite/Silicon Tandem Cells. *ACS Energy Lett.* **2016,** *1*, 474–480.
(26) Chen, H.; Wei, Z.; He, H.; Zheng, X.; Wong, K. S.; Yang, S. Solvent Engineering Boosts the Efficiency of Paintable Carbon-Based Perovskite Solar Cells to Beyond 14%. *Adv. Energy Mater.* **2016,** *6*, 1502087.
(27) Jeon, N. J.; Noh, J. H.; Kim, Y. C.; Yang, W. S.; Ryu, S.; Seok, S. I. Solvent Engineering for High-Performance Inorganic–Organic Hybrid Perovskite Solar Cells. *Nat. Mater.* **2014,** *13*, 897-903.
(28) Mao, P.; Zhou, Q.; Jin, Z.; Li, H.; Wang, J. Efficiency-Enhanced Planar Perovskite Solar Cells via an Isopropanol/Ethanol Mixed Solvent Process. *ACS Appl. Mater. Interfaces* **2016,** *8*, 23837-23843.

(29) Liang, P. W.; Liao, C. Y.; Chueh, C. C.; Zuo, F.; Williams, S. T.; Xin, X. K.; Lin, J.; Jen, A. K. Additive Enhanced Crystallization of Solution-Processed Perovskite for Highly Efficient Planar-Heterojunction Solar Cells. *Adv. Mater.* **2014,** *26*, 3748-3754.
(30) Zhang, W.; Pathak, S.; Sakai, N.; Stergiopoulos, T.; Nayak, P. K.; Noel, N. K.; Haghighirad, A. A.; Burlakov, V. M.; deQuilettes, D. W.; Sadhanala, A.; *et al.* Enhanced Optoelectronic Quality of Perovskite Thin Films with Hypophosphorous Acid for Planar Heterojunction Solar Cells. *Nat. Commun.* **2015,** *6*, 10030.
(31) Li, G.; Zhang, T.; Zhao, Y. Hydrochloric Acid Accelerated Formation of Planar $CH_3NH_3PbI_3$ Perovskite with High Humidity Tolerance. *J. Mater. Chem. A* **2015,** *3*, 19674–19678.
(32) Chang, C.-Y.; Chu, C.-Y.; Huang, Y.-C.; Huang, C.-W.; Chang, S.-Y.; Chen, C.-A.; Chao, C.-Y.; Su, W.-F. Tuning Perovskite Morphology by Polymer Additive for High Efficiency Solar Cell. *ACS Appl. Mater. Interfaces* **2015,** *7*, 4955–4961.
(33) Zhao, Y.; Wei, J.; Li, H.; Yan, Y.; Zhou, W.; Yu, D.; Zhao, Q. A Polymer Scaffold for Self-Healing Perovskite Solar Cells. *Nat. Commun.* **2016,** *7*, 10228.
(34) Wu, C.-G.; Chiang, C.-H.; Tseng, Z.-L.; Nazeeruddin, M. K.; Hagfeldt, A.; Grätzel, M. High Efficiency Stable Inverted Perovskite Solar Cells without Current Hysteresis. *Energy Environ. Sci.* **2015,** *8*, 2725-2733.
(35) Munir, R.; Sheikh, A. D.; Abdelsamie, M.; Hu, H.; Yu, L.; Zhao, K.; Kim, T.; Tall, O. E.; Li, R.; Smilgies, D.-M.; *et al.* Hybrid Perovskite Thin-Film Photovoltaics: In Situ Diagnostics and Importance of the Precursor Solvate Phases. *Adv. Mater.* **2017,** *29*, 1604113.
(36) Masi, S.; Rizzo, A.; Munir, R.; Listorti, A.; Giuri, A.; Corcione, C. E.; Treat, N. D.; Gigli, G.; Amassian, A.; Stingelin, N.; Colella, S. Organic Gelators as Growth Control Agents for Stable and Reproducible Hybrid Perovskite-Based Solar Cells. *Adv. Energy Mater.* **2017**, 1602600.
(37) Im, J.-H.; Kim, H.-S.; Park, N.-G. Morphology-Photovoltaic Property Correlation in Perovskite Solar Cells: One-Step Versus Two-Step Deposition of $CH_3NH_3PbI_3$. *APL Mater.* **2014,** *2*, 081510.
(38) Barrit, D.; Sheikh, A. D.; Munir, R.; Barbé, J. M.; Li, R.; Smilgies, D.-M.; Amassian, A. Hybrid Perovskite Solar Cells: In situ Investigation of Solution-Processed PbI_2 Reveals Metastable Precursors and a Pathway to Producing Porous Thin Films. *J. Mater. Res.* **2017,** *32*, 1899-1907.
(39) You, J.; Yang, Y. M.; Hong, Z.; Song, T.-B.; Meng, L.; Liu, Y.; Jiang, C.; Zhou, H.; Chang, W.-H.; Li, G.; *et al.* Moisture Assisted Perovskite Film Growth for High Performance Solar Cells. *Appl. Phys. Lett.* **2014,** *105*, 183902.
(40) Nie, W.; Tsai, H.; Asadpour, R.; Blancon, J.-C.; Neukirch, A. J.; Gupta, G.; Crochet, J. J.; Chhowalla, M.; Tretiak, S.; Alam, M. A.; *et al.* High-Efficiency Solution-Processed Perovskite Solar Cells with Millimeter-Scale Grains. *Science* **2015,** *347*, 522-525.
(41) Manspeaker, C.; Scruggs, P.; Preiss, J.; Lyashenko, D. A.; Zakhidov, A. A. Reliable Annealing of $CH_3NH_3PbI_3$ Films Deposited on ZnO. *J. Phys. Chem. C* **2016,** *120*, 6377−6382.
(42) Chen, J.; Cai, X.; Yang, D.; Song, D.; Wang, J.; Jiang, J.; Ma, A.; Lv, S.; Hu, M. Z.; Ni, C. Recent Progress in Stabilizing Hybrid Perovskites for Solar Cell Applications. *J. Power Sources* **2017,** *355*, 98–133.
(43) Abdelsamie, M.; Zhao, K.; Niazi, M. R.; Chou, K. W.; Amassian, A. In situ UV-Visible Absorption During Spin-Coating of Organic Semiconductors: A New Probe for Organic Electronics and Photovoltaics. *J. Mater. Chem. C* **2014,** *2*, 3373-3381.

(44) Zhou, Y.; Yang, M.; Vasiliev, A. L.; Garces, H. F.; Zhao, Y.; Wang, D.; Pang, S.; Zhu, K.; Padture, N. P. Growth Control of Compact $CH_3NH_3PbI_3$ Thin Films via Enhanced Solid-State Precursor Reaction for Efficient Planar Perovskite Solar Cells. *J. Mater. Chem. A* **2015,** *3*, 9249-9256.
(45) Zhou, Y.; Game, O. S.; Pang, S.; Padture, N. P. Microstructures of Organometal Trihalide Perovskites for Solar Cells: Their Evolution from Solutions and Characterization. *J. Phys. Chem. Lett.* **2015,** *6*, 4827-4839.
(46) Wang, Y.; Song, N.; Feng, L.; Deng, X. Effects of Organic Cation Additives on the Fast Growth of Perovskite Thin Films for Efficient Planar Heterojunction Solar Cells. *ACS Appl. Mater. Interfaces* **2016**, 8, 24703−24711.
(47) Jacobsson, T. J.; Correa-Baena, J.-P.; Anaraki, E. H.; Philippe, B.; Stranks, S. D.; Bouduban, M. E. F.; Tress, W.; Schenk, K.; Teuscher, J.; Moser, J.-E.; *et al.* Unreacted PbI_2 as a Double-Edged Sword for Enhancing the Performance of Perovskite Solar Cells. *J. Am. Chem. Soc.* **2016,** *138*, 10331–10343.
(48) Chen, Q.; Zhou, H.; Song, T.-B.; Luo, S.; Hong, Z.; Duan, H.-S.; Dou, L.; Liu, Y.; Yang, Y. Controllable Self-Induced Passivation of Hybrid Lead Iodide Perovskites toward High Performance Solar Cells. *Nano Lett.* **2014,** *14*, 4158–4163.
(49) Tennyson, E. M.; Howard, J. M.; Leite, M. S. Mesoscale Functional Imaging of Materials for Photovoltaics. *ACS Energy Let.* **2017**, *2*, 1825-1834.
(50) Garrett, J. L.; Tennyson, E. M.; Hu, M.; Huang, J.; Munday, J. N.; Leite, M. S. Real-Time Nanoscale Open-Circuit Voltage Dynamics of Perovskite Solar Cells. *Nano Let.* **2017,** *17*, 2554-2560.
(51) Hermes, I. M.; Bretschneider, S. A.; Bergmann, V. W.; Li, D.; Klasen, A.; Mars, J.; Tremel, W.; Laquai, F.; Butt, H.-J.; Mezger, M.; *et al.* Ferroelastic Fingerprints in Methylammonium Lead Iodide Perovskite. *J. Phys. Chem. C* **2016,** *120*, 5724-5731.
(52) deQuilettes, D. W.; Zhang, W.; Burlakov, V. M.; Graham, D. J.; Leijtens, T.; Osherov, A.; Bulović, V.; Snaith, H. J.; Ginger, D. S.; Stranks, S. D. Photo-Induced Halide Redistribution in Organic–Inorganic Perovskite Films. *Nat. Commun.* **2016,** *7*, 11683.
(53) Schelhas, L. T.; Christians, J. A.; Berry, J. J.; Toney, M. F.; Tassone, C. J.; Luther, J. M.; Stone, K. H. Monitoring a Silent Phase Transition in $CH_3NH_3PbI_3$ Solar Cells via Operando X-ray Diffraction. *ACS Energy Lett.* **2016,** *1*, 1007-1012.